J. Plasma Phys. (2024), *vol*. 90, 345900101
Published by Cambridge University Press
doi:10.1017/S0022377823001460

Design and construction of the near-earth space plasma simulation system of the Space Plasma Environment Research Facility

W. Ling [1], C. Jing[1], J. Wan[1], A. Mao[1], Q. Xiao[1], J. Guan[2], J. Cheng[1], C. Liu[1] and P. E[1],†

[1]Laboratory for Space Environment and Physical Sciences, Harbin Institute of Technology, Harbin 150001, PR China

[2]Department of Electrical Engineering, Harbin Institute of Technology, Harbin 150001, PR China

(Received 30 July 2023; revised 15 December 2023; accepted 18 December 2023)

Our earth is immersed in the near-earth space plasma environment, which plays a vital role in protecting our planet against the solar-wind impact and influencing space activities. It is significant to investigate the physical processes dominating the environment, for deepening our scientific understanding of it and improving the ability to forecast the space weather. As a crucial part of the National Major Scientific and Technological Infrastructure–Space Environment Simulation Research Infrastructure (SESRI) in Harbin, the Space Plasma Environment Research Facility (SPERF) builds a system to replicate the near-earth space plasma environment in the laboratory. The system aims to simulate the three-dimensional (3-D) structure and processes of the terrestrial magnetosphere for the first time in the world, providing a unique platform to reveal the physics of the 3-D asymmetric magnetic reconnection relevant to the earth's magnetopause, wave–particle interaction in the earth's radiation belt, particles' dynamics during the geomagnetic storm, etc. The paper will present the engineering design and construction of the near-earth space plasma simulation system of the SPERF, with a focus on the critical technologies that have been resolved to achieve the scientific goals. Meanwhile, the possible physical issues that can be studied based on the apparatus are sketched briefly. The earth-based system is of great value in understanding the space plasma environment and supporting space exploration.

Keywords: space plasma, magnetosphere, magnetic reconnection, wave–particle interaction, magnetic field, plasma source, plasma diagnostics, space plasma physics, plasma devices

1. Introduction

The vast majority of the observable matter of the universe has a magnetized plasma state (Mäusle 2021) showing extremely rich collective behaviours. In the solar system, all the planets are immersed in the hypersonic plasma flow blown from the sun. For the earth with an intrinsic magnetic field, a complex structure will form around it under the strike of the solar wind. This structure is named after the magnetosphere (Bamford *et al.* 2014),

† Email address for correspondence: epeng@hit.edu.cn

which deflects a substantial number of charged particles of the solar-wind plasma, thus protecting our planet from damage by them (Bamford *et al.* 2022). Despite that, coupled with the solar wind on its boundary, the magnetosphere seems highly dynamic with strong particle, momentum and energy transport, leading to several explosive phenomena such as geomagnetic storms, sub-storms (Sitnov *et al.* 2019) and energetic-electron storms (Zhou *et al.* 2013), which are detrimental to astronauts, global navigation systems, power grid systems and so forth. Therefore, it is of considerable value to study the fundamental space-plasma physical processes so as to understand the magnetosphere and forecast the space weather (Chen *et al.* 2022).

Two of the most critical physical processes in the terrestrial magnetosphere are magnetic reconnection and wave–particle interaction (Wang 2015). Magnetic reconnection at the terrestrial magnetopause is significant in importing energy of the solar wind into the magnetosphere and powering global plasma circulation (Ling *et al.* 2023*a*), and that at the magnetotail is responsible for the sub-storm dynamics and can also possibly power the geomagnetic storm (Gonzalez & Parker 2016; Angelopoulos *et al.* 2020). Wave–particle interaction is believed to be the leading cause of the active variation of the energetic electrons in the Earth's radiation belts (Thorne 2010; Zong *et al.* 2013; Artemyev *et al.* 2016, 2018; Thorne *et al.* 2021). So far, great achievements have been made for the magnetic reconnection and wave–particle interaction in the magnetosphere under comprehensive work from theoretical modelling, numerical simulation, space observation and laboratory simulation. However, there are still many key issues challenging our understanding, some of which are sketched as follows.

As for magnetic reconnection, a host of fundamental issues remain unsolved in terms of multiscale coupling, three-dimensional (3-D) physics, energy conversion, onset mechanism, turbulent reconnection, etc. Essentially, magnetic reconnection is a multiscale coupling process, but the coupling mechanism has not been clarified very well. Even though the hypotheses of plasmoid dynamics and turbulent reconnection have been proposed (Lapenta *et al.* 2018), they are not sufficiently validated due to the experimental complexity and limited computation ability (Ji & Daughton 2011; Agudelo Rueda *et al.* 2021). Meanwhile, magnetic reconnection at the terrestrial magnetopause is 3-D and asymmetrical. However, current research mainly concentrates on two-dimensional (2-D) reconnection, and 3-D reconnection physics is much less understood. For instance, the structures of the diffusion regions in 3-D (Mao *et al.* 2020) and the physical mechanisms dominating it needs profound research (Priest & Pontin 2009). Meanwhile, it is important to disclose the regimes of 3-D magnetic reconnection and their relationships in experiments (Pontin 2011), especially to elucidate the characteristics of the 3-D magnetic null points, magnetic separatrix surfaces and magnetic separators (Yamada, Kulsrud & Ji 2010; Stevenson 2015; Guo *et al.* 2022). Furthermore, the interlinked flux ropes in 3-D corresponding to the plasmoids in 2-D (Ji *et al.* 2022) are closely coupled to magnetic turbulence, but their dynamics is elusive. In addition, the issues, such as the quantitative energy conversion and partitioning process, reconnection onset as a local or global process (Pucci *et al.* 2020), the relationship between the reconnection and the turbulence, etc., have also not been addressed well for magnetic reconnection, especially for that in 3-D.

As for the wave–particle interaction, so far, theoretical models of radiation-belt dynamics mainly rely on the quasi-linear theory of wave-induced diffusion (Artemyev *et al.* 2016). However, nonlinear behaviours of the interaction between the wave and particles are important and should be included (Thorne 2010; Millan & Baker 2012; Artemyev *et al.* 2016; Thorne *et al.* 2021) when the amplitude of the wave is large. How the nonlinear wave–particle interaction influence the radiation-belt dynamics has

https://doi.org/10.1017/S0022377823001460 Published online by Cambridge University Press

to be resolved (Artemyev *et al.* 2018; Ling *et al.* 2023*b*). Whistler waves dominate in the wave–particle interaction in the radiation belt (Gu, Shprits & Ni 2012; Zhou *et al.* 2013), but they have not been understood totally. The frequency chirping of the chorus wave is suggested to be closely associated with the nonlinear resonant current driven by the electron hole in the phase space (Li *et al.* 2011). However, their relationship needs further elucidation to explain the mechanism of frequency chirping. Furthermore, it is necessary to study the influence of the inhomogeneities of the background on the whistler-wave generation and propagation (Yu *et al.* 2018; Ripoll *et al.* 2020). In addition, the relationship between the natural hiss and chorus waves is still an outstanding problem. Here, we just mentioned a small fraction of the open questions on the intriguing theme.

Nowadays, there are several ways to attack these issues in space plasma physics. In principle, the *in situ* space observation is the most appropriate one, but it has a lot of inherent limitations, such as no repeatability, uncontrollability, impossibility of global measurement, etc. Thus, theoretical modelling is adopted to explain the limited observation results based on a series of hypotheses, and computer simulation is performed to apply the theory with some unavoidable assumptions (Pontin *et al.* 2005). With the advancement of plasma-related technology, there arises a new method of studying space plasma physics, namely performing laboratory experiments. Due to the advantages in controllability, repeatability, multi-point simultaneous measurement, etc., the simulation experiment has become an important way to study fundamental space-plasma physics. Even though it is nearly impossible to reproduce the real physics in the laboratory, research on the local physics based on the similarity scaling can be used to explain what occurs in space, and the theoretical assumptions can be easily tested by the experiments. So, great advances can be made through simulation research in the laboratory.

Now, a new user facility named as SPERF (Space Plasma Environment Research Facility) is being constructed in Harbin for space plasma environment simulation. A near-earth space plasma simulation system is built on the SPERF to simulate the earth's magnetosphere (Jin *et al.* 2022*a*), thus resolving the basic space plasma physics problems, such as 3-D asymmetric magnetic reconnection, dynamics of radiation-belt charged particles (Fox & Burch 2014), geomagnetic storm, etc. Remarkably, the facility is the first device to investigate asymmetric magnetic reconnection with 3-D geometry, which is not accessible in the available facilities with 2-D magnetic geometry (Ren *et al.* 2008; Zhong *et al.* 2010; Bohlin *et al.* 2014; Olson *et al.* 2016; Hare *et al.* 2017*a*; E *et al.* 2021*a*). Meanwhile, some new regimes of magnetic reconnection can be achieved in the facility due to its large experimental region, thus allowing for research on plasmoid dynamics, kinetic instabilities and turbulent reconnection. Furthermore, the dynamic evolution of the charged particles captured in the dipole-field configuration will be studied in the facility (Ling *et al.* 2023*b*), especially focusing on wave-induced acceleration, transport and loss. The facility can also be used to probe the response of the inner magnetosphere to the magnetic-field disturbance during the geomagnetic storm (E *et al.* 2021*d*). Compared with the LDX and RT-1 devices focusing on high-β confinement and turbulent transport (Boxer *et al.* 2010; Nishiura *et al.* 2019), the boundary condition of our facility is more similar to that of the earth and the geomagnetic storm can be studied. In addition, some other problems of space plasma physics may also be studied in the facility through specific design.

Therefore, the near-earth space plasma simulation system of the SPERF aims to improve our understanding of space plasma physics. To reach the target, it is of considerable significance to achieve the magnetic field (Ling *et al.* 2022*a*), create the plasma and deploy the plasma diagnostic tools. Several challenges imposed on the engineering realization of the facility must be overcome to make it operate reliably. Here, the design and construction

https://doi.org/10.1017/S0022377823001460 Published online by Cambridge University Press

of the facility are presented, with an emphasis on explaining the critical technologies. The organization of the paper is as follows. An overview of the near-earth system of the SPERF with its scientific goals and fundamental design clarified is presented in § 2. In § 3, the design and construction of the key components of the near-earth system of the SPERF are illustrated ranging from the vacuum system, pulsed magnet system, power supply system and plasma sources to the plasma diagnostic system. Section 4 discusses the possible experiments that can be performed on the facility. Finally, § 5 summarizes the paper.

2. Project overview

As an open-user facility, the Space Plasma Environment Research Facility, abbreviated as SPERF, is dedicated to simulating the space plasma environment, including the near-earth and near-space plasma simulation systems (Jin *et al.* 2023). The near-earth space plasma simulation system (abbreviated as near-earth system) is used to simulate the 3-D structure and process of the terrestrial magnetosphere. Its main scientific goals include exploring 3-D asymmetric magnetic reconnection related to the magnetopause (Mao *et al.* 2017), studying the global dynamics of the charged particles in the artificial magnetosphere (Mao *et al.* 2020), investigating the evolution of the charged particles responding to the perturbation of the geomagnetic storm (Ling *et al.* 2023*b*) and probing the physics of the magnetic reconnection occurring at the magnetotail (Xiao *et al.* 2017).

In response to the scientific objectives, the fundamental structure of the near-earth system is designed and its main parameters are determined based on the scaling laws of physical similarity (Xiao *et al.* 2017; E *et al.* 2021*d*). Figure 1 gives the diagram of the near-earth system of the SPERF, and table 1 shows its key parameters for simulating the magnetopause 3-D magnetic reconnection and radiation belt (E *et al.* 2021*d*). A large cylindrical vacuum vessel with a length 10.5 m and radius of 2.5 m is adopted to provide an experimental region with a large spatial scale, which is crucial to simulating the magnetopause magnetic reconnection with a high Lundquist number, enlarging the effective region of the simulated radiation belt, and studying the physics in the macroscopic MHD (magnetohydrodynamic) regime. The key to replicating the physical environment of the space plasma is to simulate the plasma and magnetic field governing its dynamics (Ling *et al.* 2022*a*). To make the laboratory simulation be relevant to the real space physics, it is significant to reproduce the geometrical configuration of the simulated physical process. A group of magnets of specific structure and corresponding plasma sources are designed to meet the requirement. Four flux core magnets are used to simulate the interplanetary magnetic field and induce the laboratory solar wind, and a circular magnet is adopted to mimic the earth's dipole magnetic field (Jin *et al.* 2022*b*). The straight interplanetary magnetic field and the dipole field combine to form a 3-D geometry analogous to that of the earth's magnetopause, making it possible to study the 3-D magnetic reconnection. Two electron cyclotron resonance (ECR) sources and a cool-cathode source are designed to create the plasma for Earth's magnetosphere simulation. The 3-D magnetic reconnection is driven by the impact of the simulated solar wind against the magnetosphere built in advance through making the currents of the flux core magnets rise rapidly. When the magnetosphere is simulated separately, the wave–particle interaction and the global dynamics of the charged particles in a dipole configuration can be explored. With an extra circular magnet concentric with the dipole magnet, the magnetic disturbance during the geomagnetic storm can be simulated for studying the response of the inner magnetosphere. Additionally, combination of the dipole field and a magnetic-mirror field will create a magnetic-reconnection configuration relevant to the earth's magnetopause. In this situation, a LaB_6 plasma source is used to

https://doi.org/10.1017/S0022377823001460 Published online by Cambridge University Press

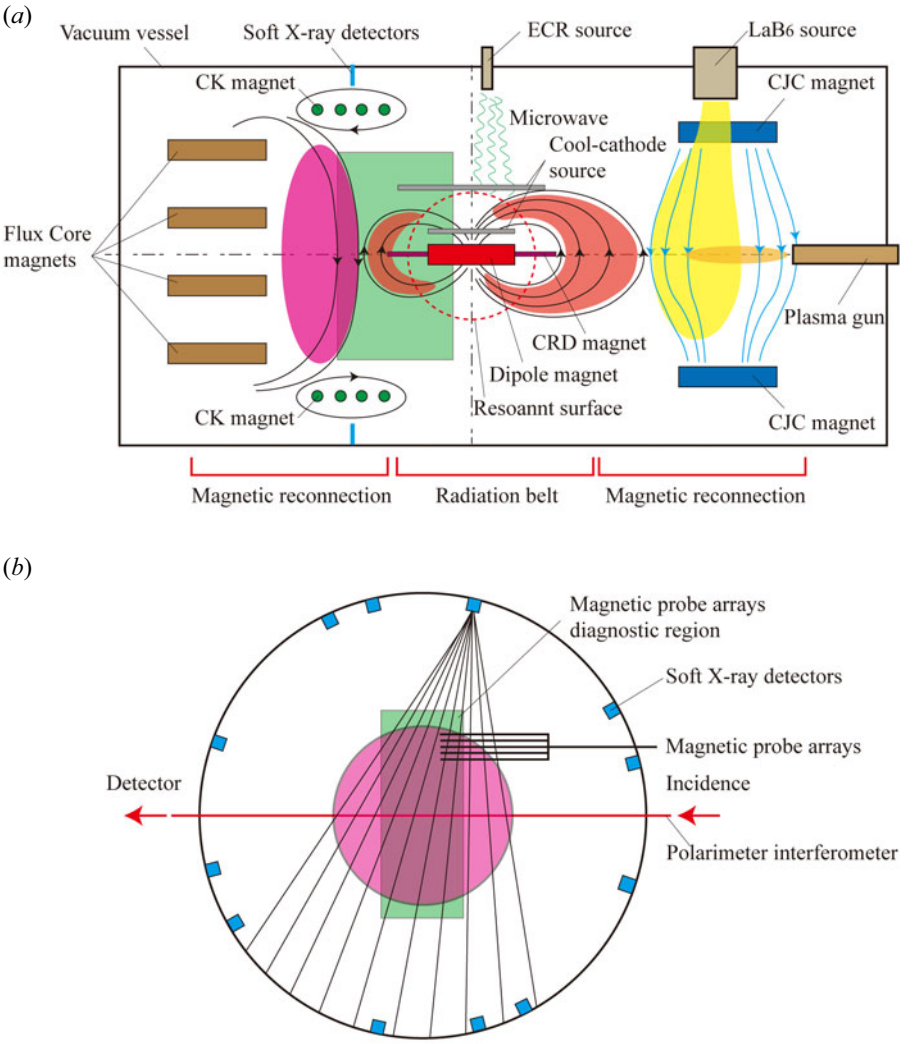

FIGURE 1. Diagram of the near-earth system of the SPERF: (*a*) front view; (*b*) side view.

simulate the magneto-sheath plasma, and the reconnection is driven by a plasma gun. Meanwhile, by using two LaB_6 plasma sources distributed symmetrically to simulate the magnetotail plasma sheets, the configuration can be easily adjusted to study the magnetotail reconnection.

Since there is an enormous difference in magnitude of the plasma characteristic parameters, such as size, magnetic field and plasma density, between the space and laboratory, it is impossible to replicate the real plasma parameters in the experimental device. However, the physics governing the space plasma can be reproduced in the laboratory with the plasma parameters scaled according to the similarity relations, which are obtained by making the dimensionless numbers in the normalized equations controlling the real and simulated plasmas constant. For magnetopause magnetic reconnection simulation, the collisionless Vlasov equations are used for the scaling and the equations of the ideal magnetohydrodynamics are applied to radiation belt simulation.

https://doi.org/10.1017/S0022377823001460 Published online by Cambridge University Press

The normalized Vlasov equations are expressed as follows:

$$\left(\frac{l_0}{v_0 t_0}\right)\frac{\partial \hat{f}_S}{\partial \hat{t}} + \hat{\boldsymbol{v}}\cdot\frac{\partial \hat{f}_S}{\partial \hat{\boldsymbol{x}}} + \left(\frac{eB_0}{m_0 v_0/l_0}\right)\frac{\hat{q}_S(\hat{\boldsymbol{E}}+\hat{\boldsymbol{v}}\times\hat{\boldsymbol{B}})}{\hat{m}}\cdot\frac{\partial \hat{f}_S}{\partial \hat{\boldsymbol{v}}} = 0, \tag{2.1}$$

$$\left(\frac{B_0}{l_0 n_0 e\mu_0 v_0}\right)\hat{\nabla}\times\hat{\boldsymbol{B}} = \int\sum_S \hat{q}_S\hat{\boldsymbol{v}}_S\hat{f}_S\,\mathrm{d}\hat{\boldsymbol{v}}_S, \tag{2.2}$$

$$\left(\frac{\varepsilon_0 E_0}{e n_0 l_0}\right)\hat{\nabla}\cdot\hat{\boldsymbol{E}} = \int\sum_S \hat{q}_S\hat{f}_S\,\mathrm{d}\hat{\boldsymbol{v}}_S, \tag{2.3}$$

where l_0, v_0, t_0, B_0, m_0, n_0 and E_0 are the characteristic length, velocity, time, magnetic field, mass, number density and electric field; e, μ_0 and ε_0 are the electron charge, vacuum permittivity and vacuum dielectric constant; $\hat{f}_S$, $\hat{t}$, $\hat{\boldsymbol{v}}$, $\hat{\boldsymbol{x}}$, $\hat{q}_S$, $\hat{\boldsymbol{E}}$, $\hat{\boldsymbol{B}}$ and $\hat{m}$ are the normalized distribution function of the charged particle of S type, time, velocity, displacement, charge, electric field, magnetic field and mass.

To retain similarity, the dimensionless numbers in the above equations should be equivalent for the space and laboratory plasmas. Denote the subscripts of the physical quantities of the space and laboratory plasmas as 01 and 02, respectively, thus

$$\frac{l_{01}}{v_{01}t_{01}} = \frac{l_{02}}{v_{02}t_{02}}, \tag{2.4}$$

$$\frac{eB_{01}}{m_{01}v_{01}/l_{01}} = \frac{eB_{02}}{m_{02}v_{02}/l_{02}}, \tag{2.5}$$

$$\frac{B_{01}}{l_{01}n_{01}e\mu_0 v_{01}} = \frac{B_{02}}{l_{02}n_{02}e\mu_0 v_{02}}, \tag{2.6}$$

$$\frac{\varepsilon_0 E_{01}}{e n_{01} l_{01}} = \frac{\varepsilon_0 E_{02}}{e n_{02} l_{02}}. \tag{2.7}$$

Suppose the scaling factors of the length and temperatures of the charged particles satisfy

$$\frac{T_{01}}{T_{02}} = \left(\frac{l_{01}}{l_{02}}\right)^{\alpha}. \tag{2.8}$$

Then, since $T_{01}\propto v_{01}^2$, $T_{02}\propto v_{02}^2$, the scaling factors of the velocity fulfil

$$\frac{v_{01}}{v_{02}} = \left(\frac{l_{01}}{l_{02}}\right)^{\alpha/2}. \tag{2.9}$$

Meanwhile, substituting this expression into (2.4)–(2.7), we can obtain that

$$\frac{t_{01}}{t_{02}} = \left(\frac{l_{01}}{l_{02}}\right)^{1-\alpha/2}, \tag{2.10}$$

$$\frac{B_{01}}{B_{02}} = \left(\frac{l_{01}}{l_{02}}\right)^{\alpha/2-1}, \tag{2.11}$$

https://doi.org/10.1017/S0022377823001460 Published online by Cambridge University Press

$$\frac{n_{01}}{n_{02}} = \left(\frac{l_{01}}{l_{02}}\right)^{-2}, \tag{2.12}$$

$$\frac{E_{01}}{E_{02}} = \left(\frac{l_{01}}{l_{02}}\right)^{-1-\alpha/2}. \tag{2.13}$$

For magnetic reconnection, there are three other parameters relevant, namely the plasma β, the inertial length d_S of the charged particle and the Lundquist number S, which are expressed as follows:

$$\beta = \frac{n_0 T_0}{B_0^2/2\mu_0}, \tag{2.14}$$

$$d_s = c\left(\frac{\epsilon_0 m_0}{n_0 q_S^2}\right)^{1/2}, \tag{2.15}$$

where c is the light speed in vacuum and q_S is the charge of the charged particle, and

$$S = \frac{\mu_0 l_0 v_A}{\eta}, \tag{2.16}$$

where v_A is the Alfvén velocity,

$$v_A = \frac{B_0}{\sqrt{\mu_0 n_0 m_i}}, \tag{2.17}$$

where m_i is the ion mass. The η is the plasma resistivity, which is proportional to $T_e^{-3/2}$. Here, T_e is the characteristic electron temperature.

With the above scaling, the β and the ratio of l_0 to d_S become constant, and S satisfies the following scaling:

$$\frac{S_1}{S_2} = \left(\frac{l_{01}}{l_{02}}\right)^{2\alpha+1}. \tag{2.18}$$

The parameters for magnetic reconnection simulation can be chosen according to these scaling relations of physical similarity. Simple computation indicates that to reach global similarity, the plasma size in the laboratory should be larger than 60 m scaled from the real size of the magnetopause ($\sim 10R_e \approx 60\ 000$ km, R_e is the earth radius). However, it is impossible to achieve this because of technology constraints. Thus, the SPERF focuses on local similarity. Table 1 shows the parameters of the real, scaled and designed parameters of the magnetosheath and the magnetosphere. Typical parameters of the magnetosheath and sub-solar magnetosphere are used in table 1 (E *et al.* 2021*d*). It should be noted that for local similarity, the size of the current layer ($\sim R_e$) of the magnetopause magnetic reconnection is used in scaling, and the ion inertial length is computed for the proton. Remarkably, to make the plasma density and magnetic field lie in appropriate ranges that can be realized in the laboratory and beneficial to diagnosis of magnetic reconnection, the scaled plasma size should be set as 6 m. Due to technology and budget limitations, the SPERF is designed to have a radius of 2.5 m, and the experimental plasma size is approximately 1.5 m. Meanwhile, the needed plasma temperatures are not easily accessible, especially for magnetosphere simulation. Nonetheless, the plasma density and magnetic field can be simulated well in the laboratory, combined with the geometry

https://doi.org/10.1017/S0022377823001460 Published online by Cambridge University Press

Physical quantity	Symbol	Magneto-sheath	Sub-solar magnetosphere	Scaled magnetosheath	Scaled sub-solar magnetosphere	Experimental magnetosheath	Experimental sub-solar magnetosphere
Plasma density	$n_e(\mathrm{cm}^{-3})$	10	1	1×10^{13}	1×10^{12}	10^{12}–10^{13}	10^{11}–10^{12}
Ion temperature	T_i (eV)	125	2000	50	800	3–10	3–10
Electron temperature	T_e (eV)	25	400	10	160	5–10	5–10
Magnetic field	B	20 nT	60 nT	126 G	380 G	100–200 G	200–400 G
Plasma β	β	1.5	0.27	1.5	0.27	0.008–0.8	3.6×10^{-4}–0.11
Length	l_0	6×10^3 km	6×10^3 km	6 m	6 m	1.5 m	1.5 m
	l_0/d_e	3.6×10^3	1.1×10^3	3.6×10^3	1.1×10^3	282–891	89–282
	l_0/d_i	83.2	26.3	83.2	26.3	6.6–20.8	2.1–6.6
Lundquist number	S	6.3×10^{10}	3.8×10^{13}	1×10^4	6.2×10^6	704–1.3×10^4	1.3×10^4–2.5×10^6

TABLE 1. Parameters for magnetic reconnection simulation.

similarity, which enables the SPERF to investigate the local physics of the magnetopause magnetic reconnection.

The normalized ideal magnetohydrodynamic equations for radiation belt simulation are given as follows:

$$\left(\frac{l_0}{t_0 u_0}\right)\frac{\partial \hat{\rho}}{\partial \hat{t}} + \hat{\nabla}\cdot(\hat{\rho}\hat{\boldsymbol{u}}) = 0, \tag{2.19}$$

$$\hat{\rho}\frac{\partial \hat{\boldsymbol{u}}}{\partial \hat{t}} + \left(\frac{u_0 t_0}{l_0}\right)\hat{\rho}\hat{\boldsymbol{u}}\cdot\hat{\nabla}\hat{\boldsymbol{u}} = -\left(\frac{P_0 t_0}{l_0\rho_0 u_0}\right)\nabla\hat{P} - \left(\frac{B_0^2 t_0}{\mu_0 l_0\rho_0 u_0}\right)\hat{\boldsymbol{B}}\times\nabla\times\hat{\boldsymbol{B}}, \tag{2.20}$$

$$\frac{\partial \hat{\boldsymbol{B}}}{\partial \hat{t}} = \left(\frac{u_0 t_0}{l_0}\right)\hat{\nabla}\times(\hat{\boldsymbol{u}}\times\hat{\boldsymbol{B}}), \tag{2.21}$$

$$\frac{\partial \hat{P}}{\partial \hat{t}} + \left(\frac{u_0 t_0}{l_0}\right)\hat{\boldsymbol{u}}\cdot\hat{\nabla}\hat{P} = -\left(\frac{u_0 t_0}{l_0}\right)\gamma\hat{P}\hat{\nabla}\cdot\hat{\boldsymbol{u}}, \tag{2.22}$$

where u_0, P_0, ρ_0 and γ are the characteristic velocity, pressure, mass density and polytropic coefficient of the plasma fluid; $\hat{\rho}$, $\hat{\boldsymbol{u}}$ and $\hat{P}$ are the normalized mass density, velocity and pressure of the plasma fluid.

Being analogous to the magnetic reconnection situation, to retain similarity, the dimensionless numbers must be identical, which means that

$$\frac{l_{01}}{t_{01}u_{01}} = \frac{l_{02}}{t_{02}u_{02}}, \tag{2.23}$$

$$\frac{P_{01}t_{01}}{l_{01}\rho_{01}u_{01}} = \frac{P_{02}t_{02}}{l_{02}\rho_{02}u_{02}}, \tag{2.24}$$

$$\frac{B_{01}^2 t_{01}}{l_{01}\rho_{01}u_{01}} = \frac{B_{02}^2 t_{02}}{l_{02}\rho_{02}u_{02}}. \tag{2.25}$$

Suppose the characteristic mass density, length and pressure satisfy the following scaling relation:

$$\frac{l_{01}}{l_{02}} = a, \quad \frac{\rho_{01}}{\rho_{02}} = b, \quad \frac{P_{01}}{P_{02}} = c. \tag{2.26a–c}$$

Then, to keep the similarity, the characteristic time, fluid velocity and magnetic field must comply with

$$\frac{t_{01}}{t_{02}} = a\sqrt{\frac{b}{c}}, \quad \frac{u_{01}}{u_{02}} = \sqrt{\frac{c}{b}}, \quad \frac{B_{01}}{B_{02}} = \sqrt{c}. \tag{2.27a–c}$$

With the scaling, the plasma β is kept constant and the Alfvén velocity transfers according to

$$\frac{V_{A1}}{V_{A2}} = \sqrt{\frac{c}{a}}. \tag{2.28}$$

Based on these scaling relations, the experimental parameters are determined and listed in table 2 (Xiao *et al.* 2017; E *et al.* 2021*d*). It is noted that the designed experimental parameters totally cover the scaled parameters. Thus, based on the geometry and parameter similarities, the radiation belt can be simulated well by the SPERF facility.

For any experimental plasma device, it is significant to perform parameter diagnosis to capture the plasma state and its evolution for physical research. Hence, multiple

https://doi.org/10.1017/S0022377823001460 Published online by Cambridge University Press

Physical quantity	Symbol	Geosynchronous orbit	Scaled parameters	Experimental parameters
Length	l_0 (m)	4×10^7	2	2
Plasma density	n_e (cm^{-3})	5	10^{12}–10^{13}	10^{12}–10^{13}
Electron temperature	T_e (eV)	(2–5) $\times$ 10^3	10–100	10–100
Ion temperature	T_i (eV)	(5–10) $\times$ 10^3	3–10	3–10
Magnetic field	B(G)	2×10^{-3}	26–355	50–400
Plasma β	β	0.35–0.75	0.35–0.75	0.003–17.7
Alfvén velocity	V_A (ms^{-1})	2×10^6	5.7×10^4–2.4×10^5	3.4×10^4–8.7×10^5

TABLE 2. Main parameters for radiation belt simulation.

plasma diagnostics tools, such as magnetic probe arrays, soft X-ray detector arrays and a polarization interferometer, are deployed in the facility to diagnose the main plasma parameters, including plasma density, electron temperature, magnetic field as well as their fluctuations. The resolutions of the diagnostic tools are needed to adapt to magnetic reconnection research. The SPERF ($\log(l_0/d_i) = 0.82$–1.3, $\log(S) = 2.8$–4.1, computed with the experimental magnetosheath parameters) lies in the single X-line collisionless regime of the magnetic reconnection phase diagram (Ji & Daughton 2011). To study physics in the electron diffusion region, the spatial resolution should be of the order of the electron skin depth of the device ($d_e = 1.7$–5.4 mm). Meanwhile, the temporal resolution is required to be higher than the Alfvén transit time, which in our facility is of the order of 1 μs.

3. Key components of the near-earth system of the SPERF

The near-earth system of the SPERF is mainly composed of the vacuum system, pulsed magnet system, pulsed power supply system, plasma source system and plasma diagnostic system. In the construction of these systems, several critical technologies have been broken through. In this section, the design and construction of these systems will be presented with the primary focus on the design goal, core parameters, crucial technical issues and solution scheme.

3.1. *Vacuum system*

The vacuum system aims to provide a pure working vacuum for the facility (Jin *et al.* 2023). To achieve the goal, an ultimate background vacuum is built first and then working gases are injected into the vacuum chamber to obtain the experimental pressure. The main challenges posed on the vacuum system lie in the fact that the vacuum vessel is large in volume, has a lot of outgassing objects in it (Jin *et al.* 2023), and possesses hundreds of interfaces on it for supporting the magnets, feeding the electrical currents into the magnets, installing the plasma sources, diagnosing the plasma, etc. As shown in figure 2, a multi-stage pumping unit is designed to achieve the ultimate background vacuum, and a pulsed gas-injection unit controlled by piezoelectric ceramic valves is adopted to establish the experimental vacuum. Meanwhile, the leakage rates of the main components in the vacuum vessel are reduced and considered in the design. The operation test shows that an ultimate vacuum of pressure at 10^{-4} Pa can be attained within 24 h based on the design, and the total leakage is smaller than 7.1×10^{-7} Pa · L s^{-1} (Jin *et al.* 2023). The reader is

https://doi.org/10.1017/S0022377823001460 Published online by Cambridge University Press

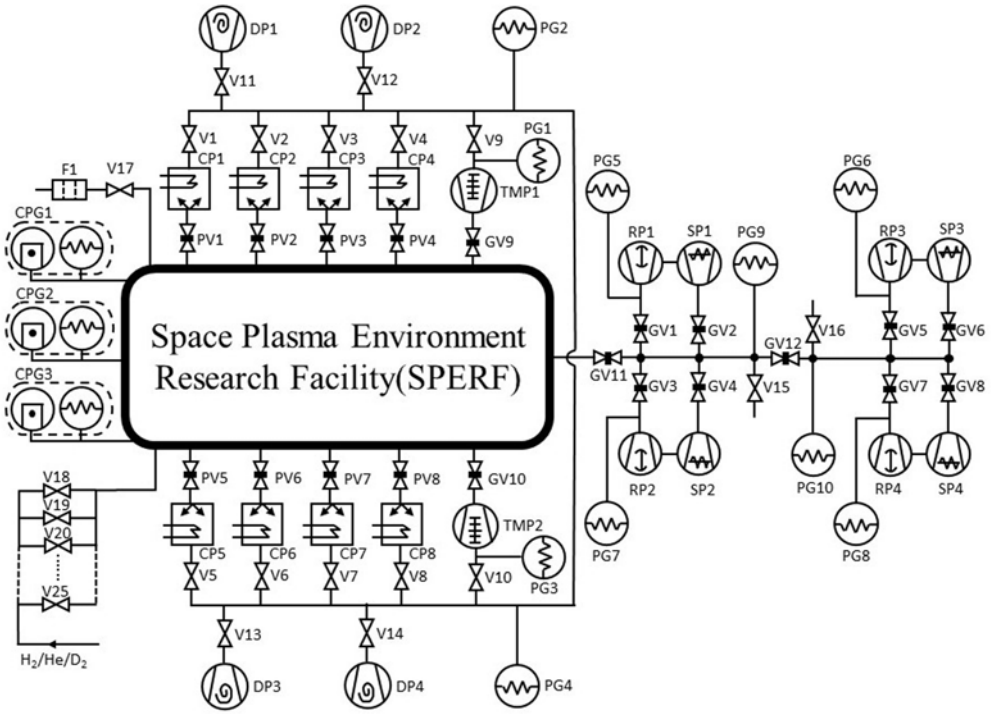

FIGURE 2. Schematic view of the vacuum system (Jin *et al.* 2023).

referred to the previous papers (Jin *et al.* 2022*a*,*b*, 2023) to grasp the technology details of the vacuum system.

3.2. *Pulsed magnet system*

Figure 3 shows the diagram of the pulsed magnet system. The structure and distribution of the magnets are designed to replicate the field geometry of the near-earth space plasma, and their parameters are dictated by the requirement of the magnetic field to keep the physical similarity. The magnet system is composed of five kinds of magnets (E *et al.* 2020), i.e. the flux core magnets, a dipole magnet, magnetopause shape-control magnets (also named CK magnets), magnetic perturbation magnets (also named CRD magnets) and magnetic mirror magnets (also named CJC magnets). Four coaxial flux core magnets, each composed of four poloidal coils (abbreviated by PF) in parallel and four toroidal coils (abbreviated by TF) in parallel, are used to simulate the solar wind. The dipole magnet creates an approximated dipole magnetic field analogous to that of the Earth. Two groups of CK magnets are employed to adjust the field topology formed by the flux core magnets and the dipole magnet to increase experimental flexibility (Ling *et al.* 2023*a*). Two CRD magnets are designed for modelling the magnetic disturbance during the geomagnetic storm. Two CJC magnets can produce a field to mimic the interplanetary magnetic field of the terrestrial magnetopause or magnetotail.

The structural and electromagnetic parameters of the magnets are designed based on the constraints in physics and technology (E *et al.* 2021*d*), such as the field geometry, magnetic field magnitude, pulsed waveform of the field, temperature rise and conductor strain (E *et al.* 2021*d*). Notably, the design of the pulsed magnet is coupled with that of the pulsed power supply, which is presented later. Table 3 shows the critical parameters

https://doi.org/10.1017/S0022377823001460 Published online by Cambridge University Press

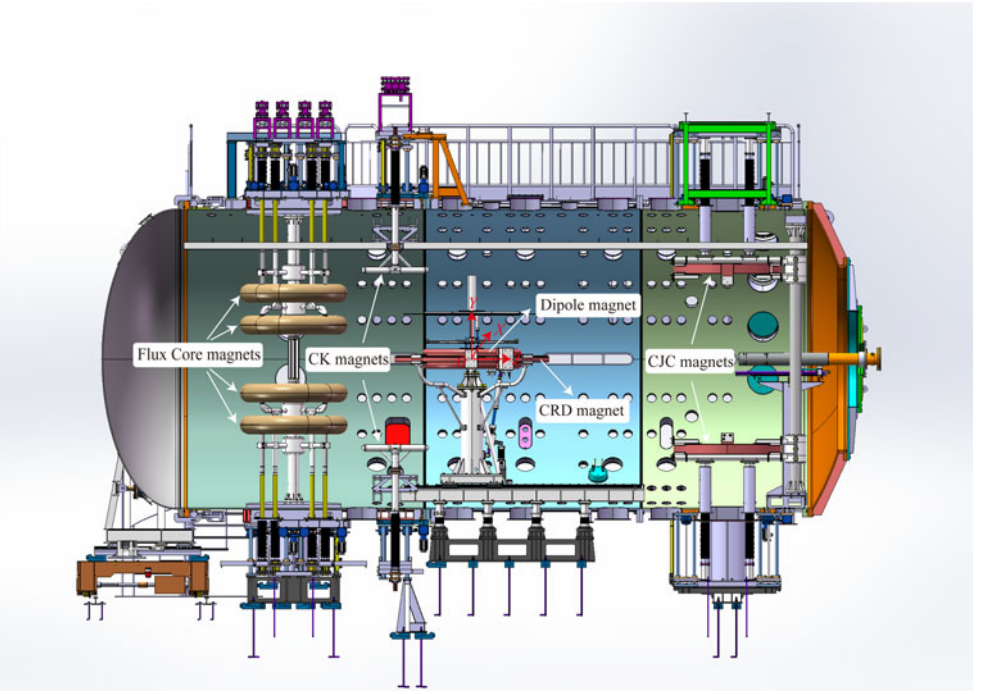

FIGURE 3. Schematic view of the pulsed magnet system (Ling *et al.* 2022*b*).

of the pulsed magnet system. Several challenges are presented to the construction of the magnets, ranging from high-voltage insulation, vacuum sealing, support and motion in vacuum, resistance to the magnetic-force impact (E *et al.* 2020), and cooling to conducting strong current through the interfaces. Many specific measures are proposed to rise to these challenges. Their details are presented in the papers continuously published in the Vacuum journal (E *et al.* 2021*e*; Ling *et al.* 2022*a*,*b*, 2023*a*,*b*). Here, we only sketch the main points of the key technologies adopted in the construction of the magnets.

The magnets can be grouped into two categories. One is the short-pulse magnet whose magnetic field reaches the target value at a typical time of the order of 0.1 ms, and the other is the long-pulse magnet that generates a magnetic field sustaining at the target value no smaller than 5 ms or 10 ms. The flux core magnets and CK magnets belong to the short-pulse magnets, and the dipole magnet and CJC magnets pertain to the long-pulse magnets. It is noted that the CRD I magnet has a short pulse, and the CRD II magnet is between the short-pulse and long-pulse magnets since its rise time can vary from 0.65 ms to 1.4 ms discretely. The short-pulse magnets except for the CRD I are all made from custom-made soft cables composed of enamel-insulated filaments for reducing the skin effect, and the long-pulse magnets and two CRD magnets are wound by the solid copper wire with a rectangular cross-section. The construction processes of the magnets are different due to the differences in their structure.

For the magnets made from the soft cables, the cables are inserted into a frame and guided through the stainless-steel tubes to the outside of the vacuum chamber. Epoxy resin is poured into the tubes for vacuum sealing, fixing the cables and improving the electrical insulation. The frame of the flux core magnets is made from G10 material. After being installed in the frame and wrapped with a layer of fibreglass tape soaked by epoxy resin (E *et al.* 2021*e*), the flux core magnets are enclosed by a thin aluminium shell for

https://doi.org/10.1017/S0022377823001460 Published online by Cambridge University Press

Magnet	Shape	Size (mm)	Conductor section (mm)	Turn×typical current (kA)	Magnetic field (G)
Flux core magnet: four PF coils	Circular	Radius 675, 695, 805, 825	Radius 12.15	1 × 360 in total	100–200 of four magnets: (1.3 m–2 m from their axis)
Flux core magnet: four TF coils	Toroidal helix	Major Radius 750, Minor radius 136	Radius 12.15	15 × 200 in total	∼1000 (centre line of the toroidal helix)
Dipole magnet	Circular	Radius 708.5	157 × 237	96 × 18	400 (2 m from the axis)
CK magnet: three groups of four sub-coils	Straight line	Each group: length 1080, interval 300	Radius 12.15	1 × 400 in total	400 of one magnet (symmetrical centre)
CRD magnet I	Circular	Radius 1200	17 × 17	1 × 132	100 (2 m from the axis)
CRD magnet II	Circular	Radius 1200	37 × 77	8 × 16	100 (2 m from the axis)
CJC magnet	Elliptical	Major axis 1278.5, Minor axis 818.5	160 × 160	64 × 8	1500 in the centre of the magnetic mirror)

TABLE 3. Critical parameters of the pulsed magnet system.

smoothing the toroidal magnetic field generated by their TF coils. Then, after being wrapped with a layer of fibreglass tape soaked by epoxy resin again (E *et al.* 2021*e*) and coated with the sol-gel coat for reducing the leakage rate, they are covered with a layer of Inconel to avoid the tip discharge that may pollute the plasma. For the CK magnets, since the frames containing their cables are stainless-steel tubes with extremely low leakage rates, there is no need for wet wrapping of fibreglass tapes and Inconel spraying.

For the magnets made from the solid conductor wire, the wire is first wound together to form a conductive body. Then, it is covered with an insulation layer relative to the ground. Notably, before this, the bodies of the dipole and CRD I magnet are embedded in a G10 frame for support. Afterwards, the magnet is addressed by the epoxy-resin impregnation method, which is important to decrease leakage, improve electrical insulation and increase mechanical strength (Ling *et al.* 2022*a*). After that, the magnet is wrapped with the sol-gel coating and followed by creating a sand layer on the outer surface of the magnet (Ling *et al.* 2022*a*). Finally, an Inconel layer is put over the surface of the magnet.

The support and motion mechanisms are specifically designed for all the magnets to bear intensive magnetic-force impact. The dipole magnet and CRD magnets are directly supported on a base that is connected to a pedestal outside the vacuum chamber through the penetration stanchions. The magnetic force exerted on the dipole magnet can be transferred to the pedestal through the stanchions without deforming the vacuum vessel. Multi-freedom motion is realized by a mechanism combining a spherical joint hinge with a guided screw, and an elastic shaft sleeve is adopted to buffer the strong magnetic-force impact (E *et al.* 2021*d*; Ling *et al.* 2022*b*). The other magnets including the flux core magnets, CK magnets and CJC magnets are all supported and moved via the supporting tubes, which go through the vacuum vessel and are fixed to and driven by a mechanism installed on the vacuum vessel. Meanwhile, buffer plates in the transverse and vertical directions are added to mitigate the strong magnetic-force impact.

For the flux core magnets and CK magnets, the cables are directly led through the vacuum vessel with an interface sealed by the solidified epoxy resin. However, for other magnets, the solid copper wires are first converted to coaxial cables, which are then changed to the solid wires penetrating the vacuum vessel. The solid wires traversing the interface are further converted to the coaxial cables to connect with the pulsed power supplies. A dedicated structure is designed to achieve transition between the soft coaxial cables and the solid copper wires or the ordinary cables. The water through the cooling channel in the wires can be separated from the electrical connection by the transition structure. During the construction of the pulsed magnet system, a series of tests in terms of high-voltage insulation, magnetic field, inductance, resistance, leakage rate and hydraulic characteristics are done to validate the design. Now, as shown in figure 4, all the magnets have been constructed and installed in the facility. First tests with operation voltage smaller than 10 kV have been done for them, and results show that the magnet system is robust to fulfil its objective.

3.3. *Pulsed power supply system*

The objective of the pulsed power supply (PPS) system is to provide excitation currents to drive the pulsed magnet system. The core challenge of the system is how to achieve two kinds of strong pulsed currents reliably, one with rise time and peak of the order of 0.1 ms and 100–600 kA, and the other with flattop time and peak of the order of 10 ms and 10–20 kA, for different inductive loads of the magnet system. The PPS generating the fast current is labelled with fast PPS and that providing the current with a flat top is marked with flat PPS. To accomplish the pulsed currents in these parameter regimes, the scheme of discharging a capacitor into an inductor with a crowbar to shape the pulse

https://doi.org/10.1017/S0022377823001460 Published online by Cambridge University Press

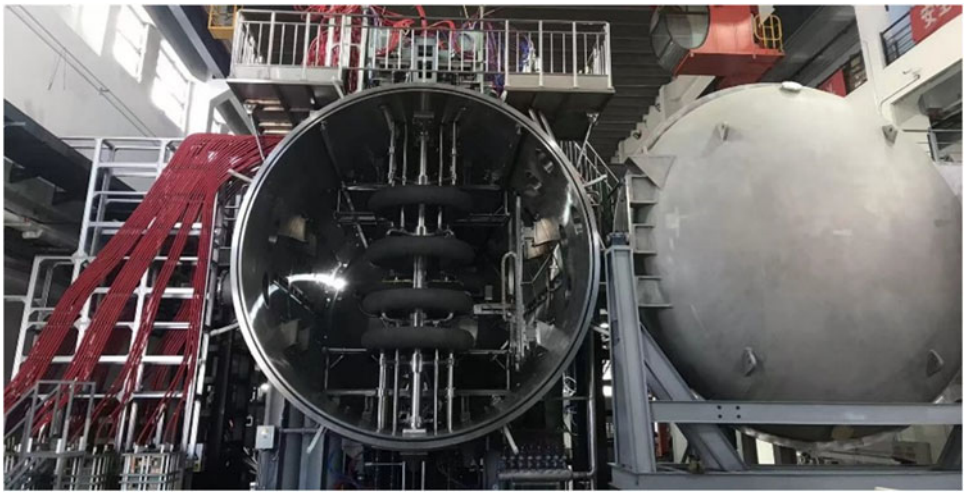

FIGURE 4. The magnet system of the SPERF.

in the descending phase is employed due to the advantages in energy density, budget, reliability, feasibility, maintenance, etc. Meanwhile, a fundamental framework based on modularization is adopted for the PPS system to improve the reliability, operation and maintenance efficiency, expandability, and flexibility of pulse forming (Mao *et al.* 2020). The module number and parameters of the capacitor and crowbar resistor are determined based on the principle of the LCR discharging circuit (Mao *et al.* 2020), and two types of modules composed of the charging unit and discharging unit are designed (E *et al.* 2021*b*).

Many critical technologies have been attacked to construct the pulsed power supply, ranging from switch assembly, crowbar branch, electromagnetic compatibility and connection of strong current. A series of papers have been published by our team to discuss these key points (Mao *et al.* 2020; E *et al.* 2021*a*,*b*,*c*; Guan *et al.* 2021*a*,*b*, 2022), and here we only summarize them simply. The thyristors are adopted as the discharging switch, which is a significant element of the pulsed power supply, due to high reliability, long lifetime and easy controllability. To conduct the strong pulsed current in the condition of high voltage, a switch assembly with five thyristors connected in series is designed along with the trigger circuit, protection circuit and monitoring unit. The thyristors with similar switch performance are used in one assembly to make them turn on synchronously, and tests have been done to validate this before integrating the assembly into the module. Meanwhile, a protective inductor between the capacitor and discharging switch has been optimized for the flat PPSs to reduce the magnitude and changing rate of the current through the thyristors to prevent them from damage by the short-circuit fault (E *et al.* 2021*b*).

The crowbar branch is composed of a diode assembly and a crowbar resistor, which is used to adjust the descending time of the current and alleviate the thermal burden of the magnet. The diode assembly is constructed by five power diodes connected in series to support the high voltage stress, and they have been chosen to have similar off-state impedance for preferable voltage-sharing performance. The crowbar resistor is optimized to be not melt by the temperature rise and have low inductance, and the cooling through forced convection of the air is adopted to raise the repetitive frequency of the PPS. Electromagnetic compatibility must be considered to reduce the influences of the electromagnetic interference (EMI) from the strong current and voltage. A distributed

https://doi.org/10.1017/S0022377823001460 Published online by Cambridge University Press

	Power supply	Number	T_{tp} (ms)	I_{tp} (kA)	T_D(μs)	W (kJ)
Fast PPSs	PF	4	0.11	360.6	599.4	1451.5
	TF	4	0.08	200.9	445.2	368.8
	CK	6	0.11	400.8	506.2	921.6
	CRD I	1	0.12	133.1	384.9	184.3
	Power supply	Number	T_{flat} (ms)	I_{tp} (kA)	T_D (ms)	W (kJ)
Flat PPSs	Dipole (separate)	1	11.57	19.02	127.95	4838.4
	Dipole (with CJC)	1	8.63	13.48	64.91	2419.2
	CJC	1	10.95	10.35	108.39	2419.2

T_{tp} and I_{tp} mean the typical time and typical current of the fast PPSs. T_{flat} and I_{peak} mean the flattop time and peak current of the flat PPSs. T_D and W stand for the descending time of the current and the PPS's stored energy. It should be noted that the CRD II PPS can provide five kinds of current with different parameters, which are not given here, and the reader can find them in the paper by Guan *et al.* (2021*b*).

TABLE 4. Parameters of the pulsed power supplies (Mao *et al.* 2020)

control system is built for the PPS with the EMI immunity done. A floating ground is used for the controller, and the coupling through distributed capacitance with the discharging circuit is mainly restrained by the isolation transformers used in the circuit powering the controller and data-acquisition elements and the optical fibre communication. Meanwhile, the original acquired voltage signal connecting to the high-voltage circuit is sent to the controller by transforming it first to the frequency signal, then to an optical signal and finally to the voltage signal. In addition, the strong pulsed current is transmitted by the coaxial cables with a shielding layer to inhibit electromagnetic interference.

The connection structure of the strong pulsed current is designed to collect the coaxial cables of the discharging modules and convert the coaxial cables to the wires of the magnets. The polarity reversal can be achieved by it, and the connection modes of the coils of the lux core magnets and CK magnets can also be changed by it. In addition, a synchronous control system with a resolution of 5 ns and a safety interlock system are designed to achieve the integrated control and operation of all the power supply modules. Based on these crucial technologies, a pulsed power supply with a total energy of 18.3 MJ has been built and passed tests on the dummy loads. Meanwhile, initial tests on the magnet system with a voltage below 10 kV show good results. Parameters of the PPSs for the pulsed magnets are shown in table 4. Figure 5 shows the physical picture of the PPS system of the SPERF.

3.4. *Plasma source system*

Several plasma sources are adopted on the SPERF near-earth system to create the plasma, including the TF coils of the flux core magnets to simulate the solar wind, two ECR plasma sources and one cool-cathode source to simulate the magnetosphere's plasma, a thermal-cathode plasma source simulating the solar wind or the plasma of the terrestrial magnetotail, and a plasma gun to drive magnetic reconnection. The parameters of these plasma sources are given in table 5. It is of extreme significance to achieve the plasmas reliably by these sources for further physical research. A lot of critical technological issues must be tackled to reach the goal, and it is necessary to optimize their performance and obtain the parameter regime before formal experiments.

https://doi.org/10.1017/S0022377823001460 Published online by Cambridge University Press

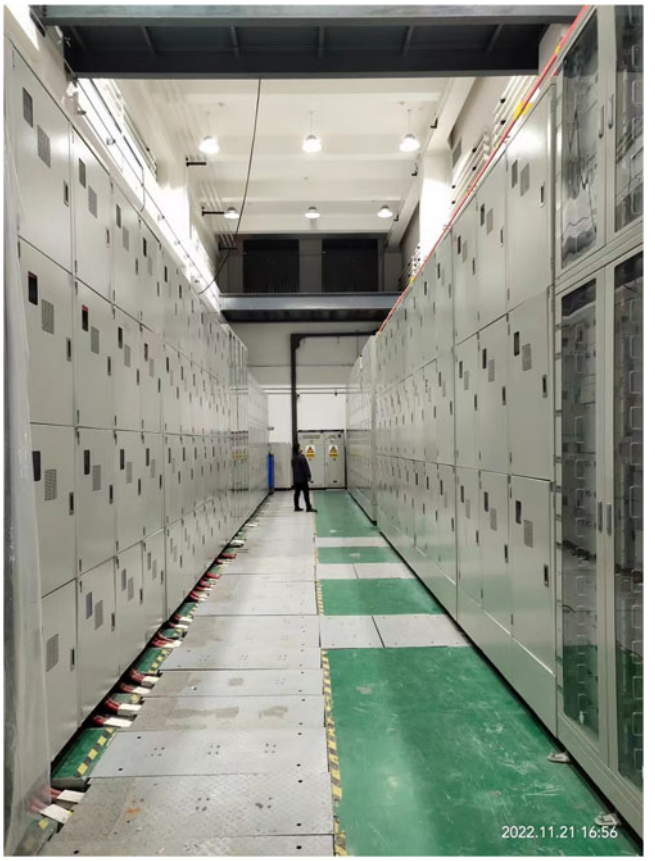

FIGURE 5. The PPS system of the SPERF.

Plasma source	Plasma density (cm^{-3})	Electron temperature (eV)	Time
Toroidal coils of the flux core magnets	10^{12}–10^{13}	5–30	>100 μs
Cool-cathode plasma source	$>10^{13}$	1–5	>1 ms
LaB_6 thermal-cathode plasma source	$>10^{13}$	3–5	>1000 s
ECR plasma source	$<5.1 \times 10^{11}$	10–100	>10 ms
Plasma gun	$>10^{12}$	1–10	>200 μs

TABLE 5. Parameters of the plasma sources on the near-earth system of the SPERF.

3.4.1. *TF coils of the flux core magnets for solar-wind plasma simulation*

The simulated solar wind is formed by the TF coils of the flux core magnets through inductive coupling (E *et al.* 2021*d*,*e*). An azimuthal electric field induced by the ramping toroidal magnetic field driven by a pulsed current through the TF coils will ionize the gas around the small circle of the flux core magnets and produce the plasma. The first plasma and its motion pushed by the poloidal field of the PF coils of the flux core magnets have been achieved (E *et al.* 2021*d*). The plasma density was measured by a probe collecting the ion saturation current in an initial test. The pressure is set as 0.5 Pa and the discharging

https://doi.org/10.1017/S0022377823001460 Published online by Cambridge University Press

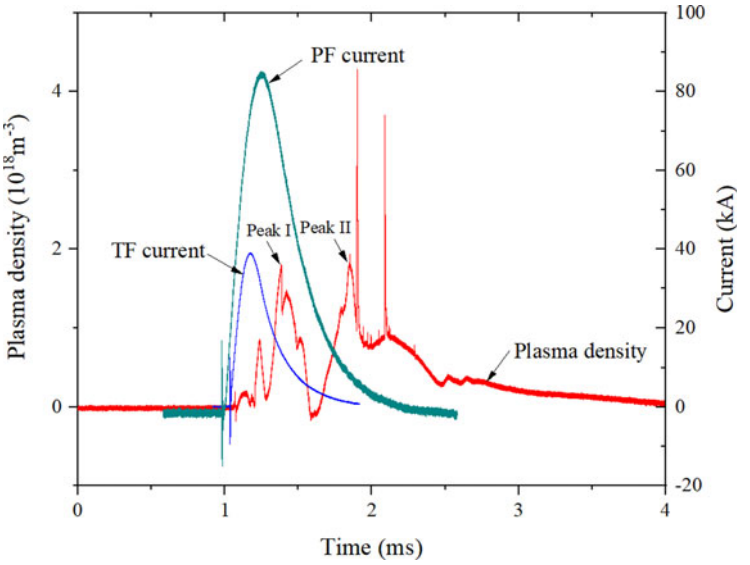

FIGURE 6. Plasma density of the TF coils.

gas is argon. Both the discharging voltages of the TF and PF coils are 3 kV, and the PF and TF coils are triggered at 1 ms and 1.05 ms, respectively. The probe is located at the axis of the SPERF, and the distance from the axis of the flux core magnets is 1.5 m. The probe's effective collection area is equal to 4.8×10^{-6} m^2. The measured plasma density and the currents of the PF and TF magnetic coils are shown in figure 6. We can see that evolution of the plasma density is complicated. The first peak of the density indicates plasma motion driven by the magnetic pressure of the PF coils and the thermal pressure of the plasma itself. Meanwhile, the second peak is believed to be caused by the outflow of the magnetic reconnection occurring between the middle two flux core magnets. The peak plasma density approaches 2×10^{18} m^{-3}, which is sufficient for magnetic reconnection research. The plasma density can be increased by improving the discharging voltages of the magnetic coils or increasing the gas pressure. Therefore, the solar-wind plasma can be modelled by the flux core magnets and it is possible to drive magnetic reconnection by pressing the plasma outward using the poloidal field of the magnets.

3.4.2. *Cool-cathode plasma source*

The simulated magnetosphere plasma is created by a cold-cathode plasma source with the ability to form a high-density ($>1 \times 10^{13}$ cm^{-3}) plasma. It consists of a round anode and a meshed cathode, which is made from molybdenum owing to its advantages of high emission efficiency of electrons, high strength and fine temperature resistance. A high-voltage pulse is exerted on the cathode relative to the anode connecting with the ground to excite glow discharge based on Paschen's law. The created plasma has a low electron temperature of 1 eV to 5 eV. The main challenge on the cool-cathode source is to trigger the plasma, and improve its stability and azimuthal uniformity (Xiao *et al.* 2017). The source will work in the prescribed dipole field of the modelled magnetosphere. Sizes of the electrodes of the cool-cathode plasma source are defined based on the magnetic field geometry to generate large-volume plasma simulating the radiation belt of the earth. The radius of the cathode and anode is designed as 1.75 m and 1.2 m, respectively, and the distance between them can be adjusted to control the region of the plasma. A capacitor-based pulsed high-voltage (up to 20 kV) supply is designed to

https://doi.org/10.1017/S0022377823001460 Published online by Cambridge University Press

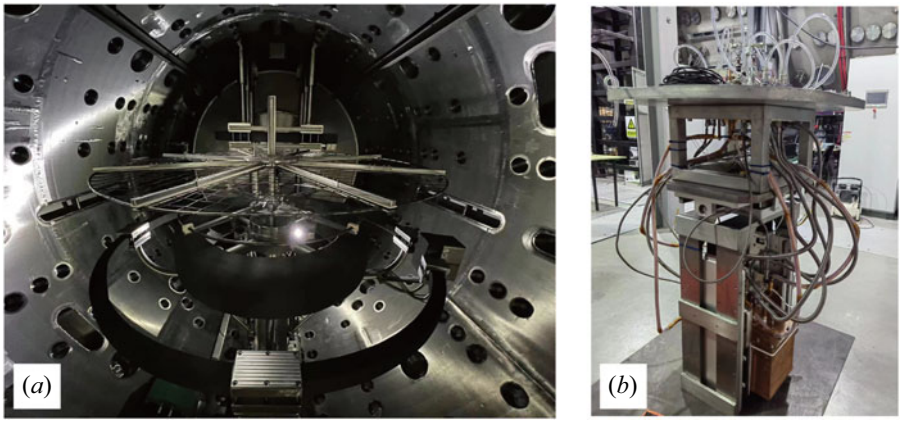

FIGURE 7. Cathode plasma sources: (*a*) cool-cathode plasma source; (*b*) thermal-cathode plasma source.

drive the source to achieve the large-volume plasma sustaining no less than 1 ms. The existence of the magnetic field may substantially increase the breakdown threshold, which can be diminished by the pre-ionization provided by an ECR plasma source which is also deployed at the SPERF. The uniformity of the plasma can be reached by making the electric field uniform through reducing the installation error and improving the smoothness of the electrodes. Now, as shown in figure 7(*a*), the cool-cathode plasma source has been constructed and integrated into the vacuum vessel, and it is being under test.

3.4.3. *LaB_6 thermal-cathode plasma source*

A LaB_6 thermal-cathode plasma source is used to generate a large-surface plasma having a density of up to 1×10^{13} cm^{-3}, which enters the experimental region by diffusion along the magnetic field. The continuous operation time of the source is required to be larger than 1000 s. The main challenge on the plasma source is to make it operate stably for a long time without fragmenting the LaB_6 cathode. The core task is to achieve enough uniform heating of the LaB_6 cathode surface. A LaB_6 cathode with a large area of 150 cm^2 (30 cm $\times$ 5 cm) is manufactured by joining many LaB_6 segments to avoid cracks due to thermal stress arising from the temperature change. To match with the design, the cathode is indirectly heated by the S-shaped tungsten wire for uniform heating. Meanwhile, a heat-shielding room is specifically designed to include the cathode to prevent heat loss. The temperature should be in the range of 1000–1500 °C to obtain a high electron-emission efficiency of the thermal cathode and impede tungsten evaporation. The plasma density is decided by the working temperature of the thermal cathode, gas condition and biased voltage of the anode. The anode is made from oxygen-free copper with high electrical and thermal conductivity, and cooling has been designed for it. In addition, the LaB_6 thermal-cathode plasma source can move in vertical and horizontal directions to change the plasma region. At present, as shown in figure 7(*b*), construction of the LaB_6 thermal-cathode plasma source has been completed, and it is now also under installation and test.

3.4.4. *ECR plasma source*

On the near-earth system of the SPERF, two ECR plasma sources are employed to generate the plasma with high electron energy, shape the plasma distribution and provide the seed electrons for the cool-cathode plasma source. Their microwave frequencies are

https://doi.org/10.1017/S0022377823001460 Published online by Cambridge University Press

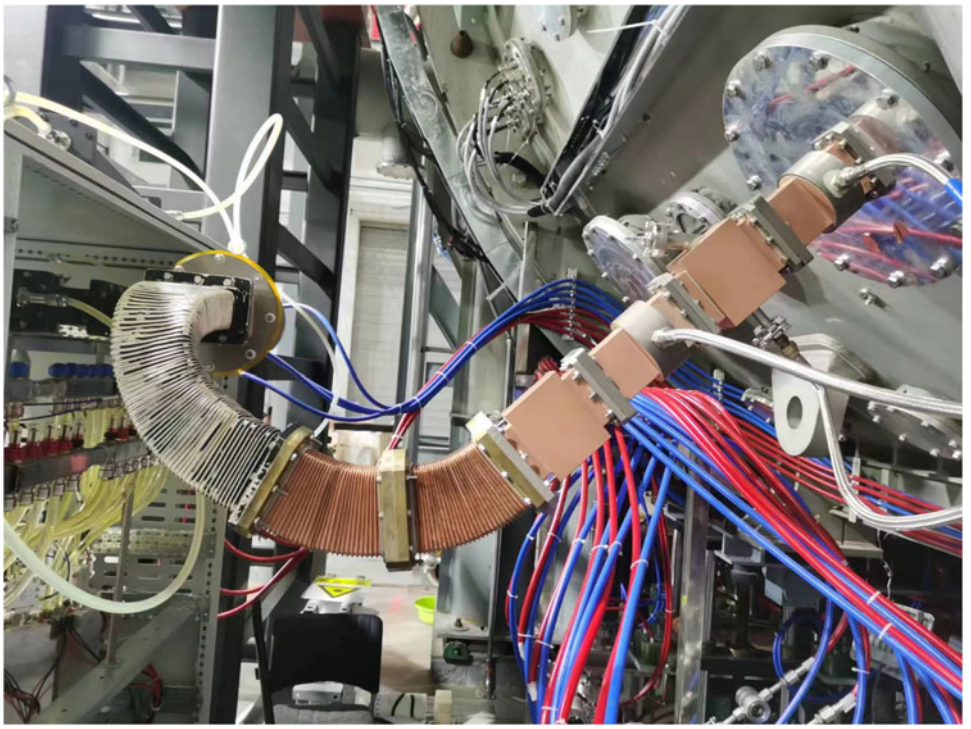

FIGURE 8. Microwave source and transfer system of the 2.45-GHz ECR plasma source.

2.45 GHz and 6.4 GHz (Xiao *et al.* 2017), and the maximum power of both sources is equal to 10 kW. The density threshold is 7.5×10^{10} cm^{-3} for the 2.45-GHz plasma source and it is 5.1×10^{11} cm^{-3} for the 6.4 GHz plasma source (Xiao *et al.* 2017). The continuous operation time of the plasma sources is needed to surpass 10 ms (E *et al.* 2021*d*). The primary challenge posed on the ECR plasma sources is how to couple the microwave power into the plasma confined in the simulated dipole field of the magnetosphere efficiently. Microwave power is mainly absorbed at the resonant surface, in which the gyrating electron resonates with the wave. For the near-earth system of the SPERF, the microwave can be absorbed by the plasma through multiple reflections on the vacuum vessel, which serves as an ideal conductor. This absorption principle is used in many similar facilities including LDX (levitated dipole experiment) (Garnier *et al.* 2006), CTX (collisionless terrella experiment) (Maslovsky, Levitt & Mauel 2003) and RT-1 (ring trap 1) (Nishiura *et al.* 2015; Ling *et al.* 2023*b*). Despite this, since the size of the vacuum vessel is large and there are many mechanical components in it, the effectiveness of this absorption mechanism may descend. Thus, to increase the microwave coupling, we designed two curved reflectometers, located above and below the dipole magnet, respectively (Ling *et al.* 2023*b*). In addition, the angle of the injecting antenna can be adjusted in the range of -5°–5° to regulate the injection direction of the microwave. Meanwhile, the plasma distribution can be shaped through adjusting the powers of two ECR sources and changing their antenna's angles. Presently, as shown in figure 8, the 2.45-GHz ECR source has been installed in the facility and is being tested. The first plasma without the arc reflectometers has been created by the 2.45-GHz plasma source successfully, and the 6.4-GHz source is under construction.

https://doi.org/10.1017/S0022377823001460 Published online by Cambridge University Press

Plasma diagnostic tools	Physical quantity	Time resolution	Spatial resolution
Single Langmuir probe	$n_e, T_e, V_p, \tilde{n}_e, \tilde{V}_p$	5 μs	<1 cm
Triple Langmuir probe	$n_e, T_e, \tilde{n}_e, \tilde{T}_e$	0.5μs	<1 cm
Magnetic probe arrays	$B, \tilde{B}$	1 μs for B	High: 2 mm
		20 ns for $\tilde{B}$	Standard: 10 mm
X-ray detectors	T_e	10 μs	∼1 cm
Polarization interferometer	$\int n_e \, \mathrm{d}s$, $\int n_e B_\parallel \, \mathrm{d}s$	<1 μs	<4 cm

n_e, T_e, V_p, B are the plasma concentration, electron temperature, plasma potential and magnetic field; the quantities with ∼ stand for the fluctuation of the corresponding equilibrium quantities; $\int n_e \, \mathrm{d}s$ and $\int n_e B_\parallel \, \mathrm{d}s$ are the chord-integrals of the n_e and $n_e B_\parallel$, where $B_\parallel$ is the magnetic field in the direction of the light chord.

TABLE 6. Main parameters of the diagnostic tools on the near-earth system of the SPERF.

3.4.5. *Plasma gun of capacitive discharge*

A plasma gun installed on the right end of the vacuum vessel is adopted to generate a hypersonic plasma jet perpendicular to the field of the magnetic-mirror magnets to drive 3-D magnetic reconnection, whose configuration is created by the dipole magnet and the magnetic mirror magnets as well as the corresponding plasmas confined by them. The plasma is accelerated out from the cavity between the coaxial electrodes of the gun under the self-consistent magnetic force. The gun has been integrated into the SPERF and tested. Test results show that the plasma is generated by the gun successfully, with a maximum plasma density larger than 1×10^{12} cm^{-3}, velocity of the plasma jet surpassing 80 km s^{-1}, diameter of the plasma with a density no smaller than 1×10^{11} cm^{-3} reaching 20 cm and plasma duration longer than 200 μs.

3.5. *Plasma diagnostic system*

Several plasma diagnostic tools are deployed on the near-earth system of the SPERF to diagnose the plasma number density, electron temperature, magnetic field and their fluctuations. The main tools of the diagnostic system adopted on the near-earth system of the SPERF, and their time and spatial resolutions are shown in table 6. The basic set-up and parameters of the system will be introduced in this section.

3.5.1. *Electrostatic probes and magnetic probe arrays*

A single probe and a triple probe are used to obtain the plasma concentration, electron temperature (Ling *et al.* 2023*b*), space potential and their fluctuations at a point with spatial resolution smaller than 1 cm. The time resolution is 5 μs and 0.5 μs, respectively. The purpose of diagnosis with the electrostatic probes is to assist in deducing the profile of the plasma distribution by analysing the chord-averaged data from the optical diagnostic instruments.

As a significant diagnostic tool for studying magnetized plasma behaviours, a group of magnetic-probe arrays is deployed on the SPERF to diagnose the magnetic field as well as its fluctuation. These arrays can be categorized into two types, namely the high-resolution array and standard-resolution array. The diagram of the two kinds of arrays is shown in figure 9(*a*). For the high-resolution array, the probes are arranged as follows. Four one-dimensional (1-D) probes are placed in the centre of the array with an interval of 2 mm, and around them, ten 3-D probes are distributed symmetrically on two sides of the array, with the first three probes 10 mm apart and the last two probes 30 mm apart on

https://doi.org/10.1017/S0022377823001460 Published online by Cambridge University Press

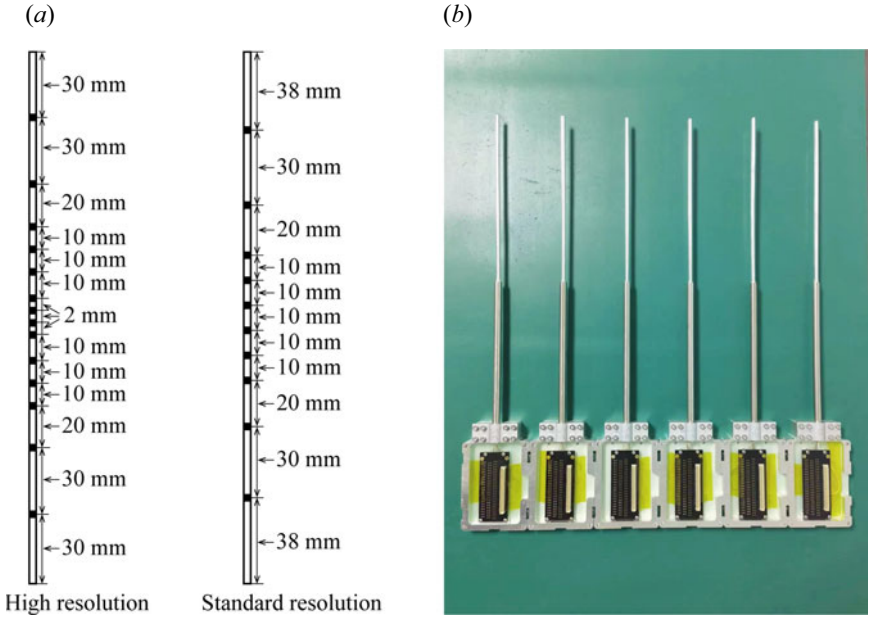

FIGURE 9. (*a*) Diagram of the magnetic-probe arrays and (*b*) their practical pictures.

one side. As to the standard-resolution array, there are ten 3-D probes in total distributed symmetrically on two sides of the array about its centre. On one side of the array, the distance of the first three probes is 10 mm and it is 30 mm for the last two probes. For both arrays, the time resolutions of measuring the magnetic field and its fluctuations are 1 μs and 20 ns, respectively, and the respective spatial resolutions for the high-resolution and standard-resolution arrays can attain 2 and 5 mm. A mechanism is designed to support five arrays 60 mm apart and change their position to achieve measurement in a large region. Figure 9(*b*) shows that the magnetic-probe arrays have been completed, and they are now under calibration and test.

3.5.2. *X-ray detectors*

The distribution of the electron temperature on the circular cross-section of the near-earth system of the SPERF is reconstructed from a group of soft X-ray detectors arranged in 12 fans, which are approximately equally spaced in angle on the circle 2.5 m in radius. Each fan includes 10 chords, and the emission along each chord is measured by two detectors blocked by respective slits, both of which has a beryllium film of different thickness for filtering. The average spatial resolution of the adjacent chords in each fan is approximately 13 cm on the central plane of the device when the width of the slits is 0.5 mm. The locations of the X-ray detectors and the chords of one fan are shown in figure 1. There are 120 channels of X-ray signals for both cases with different beryllium-film filtering, which is sufficient for the reconstruction of the 2-D emission profile. The electron temperature can be obtained by the ratio of the emissions reconstructed based on the different beryllium-film filtering. The spatial resolution of the induced electron temperature can attain a high value of approximately 1 cm. The measurable range of the electron temperature is 20–100 eV with the plasma concentration larger than 1×10^{12} cm^{-3}, and the time resolution of the diagnosis can reach 10 μs. Additionally, a FAST SDD detector is employed to probe the X-ray spectrum in the range

https://doi.org/10.1017/S0022377823001460 Published online by Cambridge University Press

of 500 eV–10 keV for analysing the emission characteristic of the plasma. The X-ray detectors are very useful in revealing the physics of magnetic reconnection and studying the transport of the energetic particles of the modelled magnetosphere.

3.5.3. *Polarization interferometer*

A far-infrared three-wave polarization interferometer is deployed for obtaining the chord-average plasma density and Faraday angle (Yang *et al.* 2021). The chord of the interferometer is in the radial direction of the near-earth system of the SPERF, and the spatial resolution of the chord is smaller than 4 cm. Now, though only one chord is designed, the system can be extended to include many chords easily in the future. The interferometer can operate in a continuous mode with a time resolution smaller than 1 μs. Three waves are generated by three solid microwave sources with frequency differences of the order of 1 MHz to approximately 320 GHz. The intermediate-frequency signal from a mixture of the left-hand and right-hand polarized probe waves contains information on the Faraday angle (Hare *et al.* 2017*b*), while the chord-average density is deduced from the intermediate-frequency signals generated by mixing the reference wave with the left-hand and right-hand circularly polarized probe waves. The Faraday angle is used to give the chord integral of the plasma density times the magnetic field in the direction of the chord. Additionally, by adjusting the location of the detectors, the signal of super-thermal collective scattering can be obtained to diagnose the plasma density fluctuation. The polarimeter-interferometer system has been constructed and now is under test and calibration.

4. Possible physical experiments

Several physical experiments are accessible in the SPERF facility. As follows, we only sketch some typical ones. The physics of 3-D asymmetric magnetic reconnection relevant to the Earth's magnetopause will be investigated at the SPERF for the first time in the world. The most important feature of the SPERF is that it can achieve the magnetic reconnection with 3-D magnetic field geometry similar to that of the terrestrial magnetopause. This enables research on physics of 3-D magnetic reconnection and expands our abilities to understand the magnetopause magnetic reconnection using controlled experiments. According to the parameters shown in table 1, the reconnection available in the facility ($(\log(L/d_i) = 0.82\text{–}1.3, \log(S) = 2.8\text{–}4.1)$ belongs to the single X-line collisionless regime of the reconnection phase diagram. Meanwhile, the ratio of the magnetic field of the simulated magnetosheath to that of the simulated sub-solar magnetosphere is equal to 0.25–1, and that of the plasma density lies in the range of 1–100. Thus, the asymmetry degree of the magnetic reconnection at the earth's magnetopause, for which the ratios of the magnetic field and plasma density between both sides of the reconnection region are approximately 0.3 and 10, respectively, can be reproduced well in the SPERF.

Several crucial physical issues in the 3-D collisionless regime of magnetic reconnection can be attacked based on the unique geometry and parameter space of the facility. The structures of the diffusion regions and the dominant physical mechanisms accounting for them for 3-D magnetic reconnection will be explored to test the validity of the theory of the multiple-layer structure that has been established well for the 2-D reconnection. Especially, it is possible to use the facility to verify the existence of the 3-D magnetic-null points, which have been observed for the magnetopause magnetic reconnection (Dunlop *et al.* 2009; Fu *et al.* 2019; Guo *et al.* 2022) but not validated in experimental devices. If the 3-D magnetic-null points can be found in the facility, related issues such as structure of the null points, conditions of their existence and physical processes governing them will be

https://doi.org/10.1017/S0022377823001460 Published online by Cambridge University Press

able to be studied. Meanwhile, even though a lot of research focuses on the dynamics of the electron diffusion region, it is still not enough to totally uncover its mystery, particularly from the perspective of the laboratory experiments. The SPERF is appropriate to study the physics of the electron diffusion region. For example, the electron pressure anisotropy is accessible to the SPERF as is done by the TREX device (Forest *et al.* 2015) so that its role on the reconnection dynamics can be investigated in the 3-D case. Furthermore, the energy conversion and partitioning process in the 3-D reconnection can be studied, which is valuable for evaluating the efficiency of energy coupling into the magnetosphere caused by the magnetic reconnection at the Earth's magnetopause. In addition, the SPERF may create turbulent reconnection due to its large experimental region, which enables research on the interaction between the wave-induce turbulence and the reconnection. In the future, the multiscale coupling issue may also be explored in the SPERF as the regime is expanded with the development of the plasma-source and diagnostic technologies.

Another crucial ability of the SPERF is to achieve the simulation of the Earth's radiation belt, which creates an environment for studying the physics relevant to the magnetosphere dynamics. The issue of the wave–particle interaction is under the central concern of scientists to explain the generation, transport and loss of the energetic particles in the magnetosphere. However, some critical points relevant to the issue wait for elaborate experimental research, some of which can be explored in the SPERF. A significant one is to study the nonlinear wave–particle interaction and its implication on the global dynamics of the radiation belt. At present, it is recognized that the whistler wave plays an essential role in the wave–particle interaction in the radiation belt, while the key physics of the wave is still elusive (Frantsuzov *et al.* 2023). The SPERF facility can be used to perform some research to bridge the gap. For example, it is possible to clarify the influence of the non-uniformity of the background magnetic field on the generation and propagation of the whistler wave. Meanwhile, the mechanism of exciting the chorus wave in the dipole configuration can also be studied in the facility. Additionally, the parameters of the facility are chosen such that the physics on the MHD scale is also accessible. Thus, the Alfvén wave can be driven in the SPERF for exploring its role in influencing the energy and momentum transport of the magnetosphere.

In addition, the facility has a unique feature to study the response of the inner magnetosphere to the magnetic disturbance during a geomagnetic storm, which has not been reported elsewhere. This function makes it possible to reveal the evolution dynamics of the energetic particles during a geomagnetic storm in the laboratory. In addition to the magnetic reconnection driven by the flux core magnets, the magnetic reconnection triggered by a plasma gun can also be achieved in the facility. The intention of this reconnection scheme is to model the magnetic reconnection at the Earth's magnetotail. The physical issues related to the magnetotail reconnection can thus be probed in the facility, one of which is the relationship between the dipolarization front and the earthward plasma jet. In summary, the SPERF will serve as an exceptional facility for research on space plasma physics due to its expanded parameter regimes and diverse functions.

5. Conclusion

The design and construction of the near-earth system of the SPERF are briefly presented in the paper. Now, the system is under a system-level cooperative test. The open facility provides a unique and comprehensive experimental platform for investigating the fundamental space plasma physical processes, such as 3-D magnetic reconnection relevant to the terrestrial magnetopause, wave–particle interaction in the dipole magnetic configuration, and particle dynamics during the geomagnetic storm through laboratory experiments. Research based on the facility will advance the developing of the global

https://doi.org/10.1017/S0022377823001460 Published online by Cambridge University Press

model of the terrestrial magnetosphere, improve our understanding of the space weather and thus aid aerospace activity. In addition, the technology accumulation ranging from the large-scale vacuum system, strong-current pulsed magnet and pulsed power supply to the large-scale plasma source can cast light on the simulation of the space plasma environment in the laboratory.

Acknowledgements

We would like to express our sincere appreciation to all the experts in the world concerning our facility and supporting its construction. Meanwhile, we are grateful to the editors and reviewers for their valuable comments. In addition, the SPERF team is gratefully acknowledged.

Editor Cary Forest thanks the referees for their advice in evaluating this article.

Declaration of interest

The authors report no conflict of interest.

Funding

This work was supported by the support of the National Key Research and Development Program of China (grant number, 2022YFA1604600) and the National Natural Science Foundation of China (P.E., grant number, 11975086), (W.L., grant number, 12305219), and Heilongjiang Postdoctoral Fund (LBH-Z22122).

REFERENCES

AGUDELO RUEDA, J.A., VERSCHAREN, D., WICKS, R.T., OWEN, C.J., NICOLAOU, G., WALSH, A.P., ZOUGANELIS, I., GERMASCHEWSKI, K. & VARGAS DOMÍNGUEZ, S. 2021 Three-dimensional magnetic reconnection in particle-in-cell simulations of anisotropic plasma turbulence. *J. Plasma Phys*. **87** (3), 905870228.

ANGELOPOULOS, V., ARTEMYEV, A., PHAN, T.D. & MIYASHITA, Y. 2020 Near-Earth magnetotail reconnection powers space storms. *Nat. Phys*. **16** (3), 317–321.

ARTEMYEV, A., AGAPITOV, O., MOURENAS, D., KRASNOSELSKIKH, V., SHASTUN, V. & MOZER, F. 2016 Oblique whistler-mode waves in the Earth's inner magnetosphere: energy distribution, origins, and role in radiation belt dynamics. *Space Sci. Rev*. **200** (1-4), 261–355.

ARTEMYEV, A.V., NEISHTADT, A.I., VASILIEV, A.A. & MOURENAS, D. 2018 Long-term evolution of electron distribution function due to nonlinear resonant interaction with whistler mode waves. *J. Plasma Phys*. **84** (2), 905840206.

BAMFORD, R., KELLETT, B., BRADFORD, J., TODD, T., BENTON, M., STAFFORD-ALLEN, R., ALVES, E., SILVA, L., COLLINGWOOD, C., CRAWFORD, I., *et al.* 2014 An exploration of the effectiveness of artificial mini-magnetospheres as a potential solar storm shelter for long term human space missions. *Acta Astronaut*. **105** (2), 385–394.

BAMFORD, R., KELLETT, B., GREEN, J., DONG, C., AIRAPETIAN, V. & BINGHAM, R. 2022 How to create an artificial magnetosphere for Mars. *Acta Astronaut*. **190**, 323–333.

BOHLIN, H., VON STECHOW, A., RAHBARNIA, K., GRULKE, O. & KLINGER, T. 2014 VINETA II: a linear magnetic reconnection experiment. *Rev. Sci. Instrum*. **85** (2), 023501.

BOXER, A.C., BERGMANN, R., ELLSWORTH, J.L., GARNIER, D.T., KESNER, J., MAUEL, M.E. & WOSKOV, P. 2010 Turbulent inward pinch of plasma confined by a levitated dipole magnet. *Nat. Phys*. **6** (3), 207–212.

CHEN, X., ZHANG, H., ZONG, Q., ZHOU, X., ZOU, H., WANG, Y. & YUE, C. 2022 Non-adiabatic acceleration of injected electrons in the inner magnetosphere: joint observations by the Van Allen Probe and the BeiDa Imaging Electron Spectrometer. *Geophys. Res. Lett*. **49** (21).

Dunlop, M.W., Zhang, Q., Xiao, C., He, J., Pu, Z., Fear, R.C., Shen, C. & Escoubet, C.P. 2009 Reconnection at high latitudes: antiparallel merging. *Phys. Rev. Lett*. **102** (7), 075005.

E, P., Guan, J., Jin, C., Mao, A., Ma, X., Deng, W., Ding, M., Kang, C., Li, S., Xiao, J., *et al.* 2021*a* An 18.3 MJ charging and discharging pulsed power supply system for the Space Plasma Environment Research Facility (SPERF): the subsystem for the magnetopause shape control coils. *Rev. Sci. Instrum*. **92** (6), 064709.

E, P., Guan, J., Ling, W., Ma, X., Mao, A., Deng, W., Ding, M., Li, S., Kang, C. & Li, H. 2021*b* An 18.3 MJ charging and discharging pulsed power supply system for the Space Plasma Environment Research Facility (SPERF): modular design method and component selection. *Rev. Sci. Instrum*. **92** (3), 034709.

E, P., Guan, J., Ma, X., Mao, A., Deng, W., Ding, M., Kang, C., Li, S., Xiao, J. & Li, H. 2021*c* An 18.3 MJ charging and discharging pulsed power supply system for the Space Plasma Environment Research Facility (SPERF): the subsystem for the dipole coil. *Rev. Sci. Instrum*. **92** (4), 044706.

E, P., Ling, W., Mao, A., Jin, C., Xiao, Q., Xu, F., Chen, C., Bai, X., Hao, H., Lu, Y., *et al.* 2021*d* The magnet system of the Space Plasma Environment Research Facility (SPERF): parameter design and electromagnetic analysis. *Rev. Sci. Instrum*. **92** (4), 044709.

E, P., Ling, W., Mao, A., Jin, C., Zhu, G., Tan, L., Chen, C. & Lu, Y. 2021*e* Design and construction of the Flux Core coils of the Space Plasma Environment Research Facility (SPERF). *Vacuum* **192**, 110468.

E, P., Ling, W., Mao, A., Xiao, Q., Guan, J. & Zhang, Z. 2020 Study on the magnetic forces of the dipole in the SPERF. *IEEE Trans. Plasma Sci*. **48** (1), 266–274.

Forest, C., Flanagan, K., Brookhart, M., Clark, M., Cooper, C.M., Désangles, V., Egedal, J., Endrizzi, D., Khalzov, I.V., Li, H., *et al.* 2015 The Wisconsin plasma astrophysics laboratory. *J. Plasma Phys*. **81** (5), 345810501.

Fox, N. & Burch, J.L. (Ed.) 2014 *The Van Allen Probes Mission*, 1st edn. Springer.

Frantsuzov, V.A., Artemyev, A.V., Zhang, X.-J., Allanson, O., Shustov, P.I. & Petrukovich, A.A. 2023 Diffusive scattering of energetic electrons by intense whistler-mode waves in an inhomogeneous plasma. *J. Plasma Phys*. **89** (1), 905890101.

Fu, H.S., Cao, J.B., Cao, D., Wang, Z., Vaivads, A., Khotyaintsev, Y.V., Burch, J.L. & Huang, S.Y. 2019 Evidence of magnetic nulls in electron diffusion region. *Geophys. Res. Lett*. **46** (1), 48–54.

Garnier, D., Hansen, A., Kesner, J., Mauel, M., Michael, P., Minervini, J., Radovinsky, A., Zhukovsky, A., Boxer, A., Ellsworth, J., *et al.* 2006 Design and initial operation of the LDX facility. *Fusion Engng Des*. **81** (20-22), 2371–2380.

Gonzalez, W. & Parker, E. (Ed.) 2016 *Magnetic Reconnection: Concepts and Applications*, 1st edn., Astrophysics and Space Science Library, vol. 427. Springer (Imprint).

Gu, X., Shprits, Y.Y. & Ni, B. 2012 Parameterized lifetime of radiation belt electrons interacting with lower-band and upper-band oblique chorus waves: parameterization of electron lifetimes. *Geophys. Res. Lett*. **39** (15).

Guan, J., E, P., Ma, X., Mao, A., Deng, W., Ding, M., Kang, C., Li, S., Xiao, J., Tong, W., *et al.* 2021*a* An 18.3-MJ charging and discharging pulsed power supply system for the Space Plasma Environment Research Facility (SPERF): the subsystem for the magnetosheath coils. *Rev. Sci. Instrum*. **92** (8), 084701.

Guan, J., E, P., Mao, A., Ma, X., Jin, C., Deng, W., Ding, M., Li, S., Kang, C., Xiao, J., *et al.* 2021*b* An 18.3 MJ charging and discharging pulsed power supply system for the Space Plasma Environment Research Facility (SPERF): the subsystem for the magnetic perturbation coils. *Rev. Sci. Instrum*. **92** (9), 094706.

Guan, J., Ling, W., Ma, X., Li, H., Tong, W. & E, P. 2022 Design of pulsed current source for Toroidal Field coils in SPERF. *J. Power Supply* **20** (6), 154–183.

Guo, R., Pu, Z., Wang, X., Xiao, C. & He, J. 2022 3D reconnection geometries with magnetic nulls: multispacecraft observations and reconstructions. *J. Geophys. Res.: Space Phys*. **127** (2).

Hare, J.D., Lebedev, S.V., Suttle, L.G., Loureiro, N.F., Ciardi, A., Burdiak, G.C., Chittenden, J.P., Clayson, T., Eardley, S.J., Garcia, C., *et al.* 2017*b* Formation and

structure of a current sheet in pulsed-power driven magnetic reconnection experiments. *Phys. Plasmas* **24** (10), 102703.

HARE, J., SUTTLE, L., LEBEDEV, S., LOUREIRO, N., CIARDI, A., BURDIAK, G., CHITTENDEN, J., CLAYSON, T., GARCIA, C., NIASSE, N., *et al.* 2017*a* Anomalous heating and plasmoid formation in a driven magnetic reconnection experiment. *Phys. Rev. Lett*. **118** (8), 085001.

JI, H. & DAUGHTON, W. 2011 Phase diagram for magnetic reconnection in heliophysical, astrophysical, and laboratory plasmas. *Phys. Plasmas* **18** (11), 111207.

JI, H., DAUGHTON, W., JARA-ALMONTE, J., LE, A., STANIER, A. & YOO, J. 2022 Magnetic reconnection in the era of exascale computing and multiscale experiments. *Nat. Rev. Phys*. **4** (4), 263–282.

JIN, C., ZHANG, Y., LING, W., CHEN, C., WANG, H., HAO, H., DONG, Y., LU, Y., LI, L. & E, P. 2023 Vacuum system of the Space Plasma Environment Research Facility. *J. Vac. Sci. Technol.* B **41** (3), 034204.

JIN, C., ZHANG, Y., LING, W., LIU, M., E, P., CHEN, C., LI, Y., PENG, Z., LU, Y. & LI, L. 2022*a* Vacuum control system for the Space Plasma Environment Research Facility. *J. Vac. Sci. Technol.* B **40** (3), 034201.

JIN, C., ZHANG, Y., LING, W., YANG, X., CHENG, J., FENG, L., WAN, J., WANG, H., LU, Y., LI, L., *et al.* 2022*b* Design of the vacuum-centralized control system for the space plasma environment research facility based on the Experimental Physics and Industrial Control System. *J. Vac. Sci. Technol.* B **40** (4), 044202.

LAPENTA, G., PUCCI, F., OLSHEVSKY, V., SERVIDIO, S., SORRISO-VALVO, L., NEWMAN, D.L. & GOLDMAN, M.V. 2018 Nonlinear waves and instabilities leading to secondary reconnection in reconnection outflows. *J. Plasma Phys*. **84** (1), 715840103.

LI, W., BORTNIK, J., THORNE, R.M. & ANGELOPOULOS, V. 2011 Global distribution of wave amplitudes and wave normal angles of chorus waves using THEMIS wave observations: chorus wave distribution on THEMIS. *J. Geophys. Res*. **116**, A12205.

LING, W., JIN, C., E, P., ZHU, G., XU, F., CHEN, C., LU, Y., WU, J. & LI, L. 2022*a* Design and construction of the magnetic mirror magnets of the space plasma environment research facility (SPERF). *Vacuum* **205**, 111402.

LING, W., JIN, C., MAO, A., E, P., WU, J., ZHU, G., CHEN, C., LU, Y.-W. & LI, L. 2022*b* Design and construction of the dipole magnet of the space plasma environment research facility (SPERF) for simulating the earth magnetosphere. *Vacuum* **201**, 111112.

LING, W., JIN, C., YIN, M., GUAN, J., ZHU, G., XU, F., CHEN, C., LU, Y., WU, J., LI, L., *et al.* 2023*a* Design and construction of the magnetopause shape control coils of the Space Plasma Environment Research Facility to regulate the field configuration of the simulated Earth's magnetopause magnetic reconnection. *Vacuum* **212**, 111975.

LING, W., JIN, C., ZHU, G., XU, F., CHEN, C., LU, Y., WU, J., LI, L. & E, P. 2023*b* Design and construction of the magnetic perturbation magnets of the space plasma environment research facility for simulating the geomagnetic storm on the ground. *Vacuum* **209**, 111756.

MAO, A., MA, X., E, P., GUAN, J., LING, W., LI, L. & LI, H. 2020 An 18.3 MJ charging and discharging pulsed power supply system for the Space Plasma Environment Research Facility (SPERF). I. The overall design. *Rev. Sci. Instrum*. **91** (8), 084702.

MAO, A., REN, Y., JI, H., E, P., HAN, K., WANG, Z., XIAO, Q. & LI, L. 2017 Conceptual design of the three-dimensional magnetic field configuration relevant to the magnetopause reconnection in the SPERF. *Plasma Sci. Technol*. **19** (3), 034002.

MASLOVSKY, D., LEVITT, B. & MAUEL, M.E. 2003 Observation of nonlinear frequency-sweeping suppression with rf diffusion. *Phys. Rev. Lett*. **90** (18), 185001.

MÄUSLE, R. 2021 Investigation of topology-driven magnetic reconnection with CWENO finite volume numerics. Master's thesis, Freie Universität Berlin.

MILLAN, R.M. & BAKER, D.N. 2012 Acceleration of particles to high energies in Earth's radiation belts. *Space Sci. Rev*. **173** (1-4), 103–131.

Nishiura, M., Yoshida, Z., Kenmochi, N., Sugata, T., Nakamura, K., Mori, T., Katsura, S., Shirahata, K. & Howard, J. 2019 Experimental analysis of self-organized structure and transport on the magnetospheric plasma device RT-1. *Nucl. Fusion* **59** (9), 096005.

Nishiura, M., Yoshida, Z., Saitoh, H., Yano, Y., Kawazura, Y., Nogami, T., Yamasaki, M., Mushiake, T. & Kashyap, A. 2015 Improved beta (local beta >1) and density in electron cyclotron resonance heating on the RT-1 magnetosphere plasma. *Nucl. Fusion* **55** (5), 053019.

Olson, J., Egedal, J., Greess, S., Myers, R., Clark, M., Endrizzi, D., Flanagan, K., Milhone, J., Peterson, E., Wallace, J., *et al.* 2016 Experimental demonstration of the collisionless plasmoid instability below the ion kinetic scale during magnetic reconnection. *Phys. Rev. Lett*. **116** (25), 255001.

Pontin, D. 2011 Three-dimensional magnetic reconnection regimes: a review. *Adv. Space Res*. **47** (9), 1508–1522.

Pontin, D.I., Galsgaard, K., Hornig, G. & Priest, E.R. 2005 A fully magnetohydrodynamic simulation of three-dimensional non-null reconnection. *Phys. Plasmas* **12** (5), 052307.

Priest, E.R. & Pontin, D.I. 2009 Three-dimensional null point reconnection regimes. *Phys. Plasmas* **16** (12), 122101.

Pucci, F., Velli, M., Shi, C., Singh, K.A.P., Tenerani, A., Alladio, F., Ambrosino, F., Buratti, P., Fox, W., Jara-Almonte, J., *et al.* 2020 Onset of fast magnetic reconnection and particle energization in laboratory and space plasmas. *J. Plasma Phys*. **86** (6), 535860601.

Ren, Y., Yamada, M., Ji, H., Gerhardt, S.P. & Kulsrud, R. 2008 Identification of the electron-diffusion region during magnetic reconnection in a laboratory plasma. *Phys. Rev. Lett*. **101** (8), 085003.

Ripoll, J., Claudepierre, S.G., Ukhorskiy, A.Y., Colpitts, C., Li, X., Fennell, J.F. & Crabtree, C. 2020 Particle dynamics in the Earth's radiation belts: review of current research and open questions. *J. Geophys. Res. Space Phys*. **125** (5).

Sitnov, M., Birn, J., Ferdousi, B., Gordeev, E., Khotyaintsev, Y., Merkin, V., Motoba, T., Otto, A., Panov, E., Pritchett, P., *et al.* 2019 Explosive magnetotail activity. *Space Sci. Rev*. **215** (4), 31.

Stevenson, J.E. 2015 On the properties of single-separator MHS equilibria and the nature of separator reconnection. PhD thesis, University of St Andrews.

Thorne, R.M. 2010 Radiation belt dynamics: he importance of wave-particle interactions. *Geophys. Res. Lett*. **37** (22), L22107.

Thorne, R.M., Bortnik, J., Li, W. & Ma, Q. 2021 Wave-particle interactions in the Earth's magnetosphere. In *Geophysical Monograph Series*, 1st edn (ed. R. Maggiolo, N. André, H. Hasegawa, D.T. Welling, Y. Zhang & L.J. Paxton), pp. 93–108. Wiley.

Wang, Y. 2015 Recent advances in radiation belt dynamics and wave-particle interactions in the Earth's inner magnetosphere. *Sci. China Earth Sci*. **58** (12), 2355–2356.

Xiao, Q., Wang, Z., Wang, X., Xiao, C., Yang, X. & Zheng, J. 2017 Conceptual design of Dipole Research Experiment (DREX). *Plasma Sci. Technol*. **19** (3), 035301.

Yamada, M., Kulsrud, R. & Ji, H. 2010 Magnetic reconnection. *Rev. Mod. Phys*. **82** (1), 603–664.

Yang, Q., Gao, L., Shi, P., Zhou, Y., Wang, Y. & Zhou, C. 2021 Upgrade of far infrared three-wave polarimeter–interferometer system on Joint-TEXT. *Rev. Sci. Instrum*. **92** (5), 053527.

Yu, Y., Delzanno, G.L., Jordanova, V., Peng, I.B. & Markidis, S. 2018 PIC simulations of wave-particle interactions with an initial electron velocity distribution from a kinetic ring current model. *J. Atmos. Sol.-Terr. Phys*. **177**, 169–178.

Zhong, J., Li, Y., Wang, X., Wang, J., Dong, Q., Xiao, C., Wang, S., Liu, X., Zhang, L., An, L., *et al.* 2010 Modelling loop-top X-ray source and reconnection outflows in solar flares with intense lasers. *Nat. Phys*. **6** (12), 984–987.

Zhou, X., Xiao, F., He, Y., Yang, C., Zhou, Q., Zhang, Z., Gao, Z. & Ding, Y. 2013 Responses of geostationary orbit energetic electron fluxes to chorus waves under different geomagnetic conditions. *Sci. China Earth Sci*. **56** (12), 2006–2014.

Zong, Q., Yuan, C., Wang, Y. & Su, Z. 2013 Dynamic variation and the fast acceleration of particles in Earth's radiation belt. *Sci. China Earth Sci*. **56** (7), 1118–1140.